nanomaterials

MDPI

Article

Highly Efficient and Stable Self-Powered Perovskite Photodiode by Cathode-Side Interfacial Passivation with Poly(Methyl Methacrylate)

Wonsun Kim [1], JaeWoo Park [2], Yushika Aggarwal [1], Shital Sharma [2], Eun Ha Choi [1,2] and Byoungchoo Park [1,2,*]

[1] Department of Electrical and Biological Physics, Kwangwoon University, Seoul 01897, Republic of Korea
[2] Department of Plasma-Bio Display, Kwangwoon University, Seoul 01897, Republic of Korea
* Correspondence: bcpark@kw.ac.kr; Tel.: +82-2-940-5237

Abstract: For several years now, organic–inorganic hybrid perovskite materials have shown remarkable progress in the field of opto-electronic devices. Herein, we introduce a cathode-side passivation layer of poly(methyl methacrylate) (PMMA) for a highly efficient and stable self-powered $CH_3NH_3PbI_3$ perovskite-based photodiode. For effective noise–current suppression, the PMMA passivation layer was employed between a light-absorbing layer of $CH_3NH_3PbI_3$ ($MAPbI_3$) perovskite and an electron transport layer of [6,6]-phenyl-C61-butyric acid methyl ester. Due to its passivation effect on defects in perovskite film, the PMMA passivation layer can effectively suppress interface recombination and reduce the leakage/noise current. Without external bias, the $MAPbI_3$ photodiode with the PMMA layer demonstrated a significantly high specific detectivity value (~1.07×10^{12} Jones) compared to that of a conventional $MAPbI_3$ photodiode without a PMMA layer. Along with the enhanced specific detectivity, a wide linear dynamic response (~127 dB) with rapid rise (~50 μs) and decay (~17 μs) response times was obtained. Furthermore, highly durable dynamic responses of the PMMA-passivated $MAPbI_3$ photodiode were observed even after a long storage time of 500 h. The results achieved with the cathode-side PMMA-passivated perovskite photodiodes represent a new means by which to realize highly sensitive and stable self-powered photodiodes for use in developing novel opto-electronic devices.

Keywords: photodetector; polymeric passivation layer; organic/inorganic hybrid perovskite

Citation: Kim, W.; Park, J.W.; Aggarwal, Y.; Sharma, S.; Choi, E.H.; Park, B. Highly Efficient and Stable Self-Powered Perovskite Photodiode by Cathode-Side Interfacial Passivation with Poly(Methyl Methacrylate). *Nanomaterials* **2023**, *13*, 619. https://doi.org/10.3390/nano13030619

Academic Editors: Qiongfeng Shi, Jianxiong Zhu and Julia Pérez-Prieto

Received: 19 January 2023
Revised: 29 January 2023
Accepted: 1 February 2023
Published: 3 February 2023

1. Introduction

Energy-harvesting photovoltaic (PV) technologies based on hybrid organic/inorganic perovskite materials have attracted the interest of many research groups due to the excellent optoelectronic characteristics, high charge carrier mobility, tunable bandgaps, and high diffusion ranges of these materials. Moreover, they are simple, operate at low temperatures, are solution processability, and have a low fabrication cost [1–6]. Given these characteristics, hybrid organic/inorganic perovskite materials are utilized in various optoelectronic devices such as PV or solar cells, light-emitting diodes, and especially in photodetectors [7–9]. In recent years, $CH_3NH_3PbI_3$ ($MAPbI_3$) organohalide perovskite photodetectors have shown significantly increased photo-detecting capabilities with rapid response times, with detectivity (D^*) values of ~7.8×10^{12} Jones (Jones = cm $Hz^{1/2}$/W) and responsivity (R) values close to 470 mA/W [10–13]. These results are slightly lower than or comparable to those of conventional silicon photodetectors (D^* ~1×10^{13} Jones) [14].

Despite the advent of these new types of device structures and novel materials for improving the performance capabilities of perovskite-based devices, deeply rooted problems including defect-rich and distorted lattice structures in the bulk and surfaces of the $MAPbI_3$ perovskite layers remain unsolved [15–20]. Specifically, defects in perovskite layers hamper the charge transport and extraction processes, causing interfacial recombination losses between the light-absorbing layer and adjacent charge transport layers and/or

electrodes [17–20]. Due to these losses, much work remains for further improvements of the optoelectronic device performance and stability over conventional silicon-based devices [21,22].

Among the attempts to improve the interface quality of perovskite layers in PV cells, passivation layers consisting of functional organics or polymers such as poly(ethylene oxide) and poly(methyl methacrylate) (PMMA) have been suggested and successfully demonstrated. These were found to possess effective interface engineering based on their chemical and physical/electrical advantages [17–19,23,24]. Recently, the present authors also showed a self-powered $MAPbI_3$ perovskite-based photodiode device with an anode-side passivation layer of PMMA at the interface between a $MAPbI_3$ light-absorbing layer and a hole-transport layer (HTL) [25]. The anode-side PMMA passivation layer could reduce carrier recombination losses and noise currents. Thus, high specific detectivity (~0.81×10^{12} Jones) was achieved even without external bias [25].

Nonetheless, the introduction of a PMMA passivation layer between the light-absorbing layer and the electron-transport layer (ETL) for perovskite photodiodes has not been fully investigated and remains poorly understood [9,20]. Unlike the formation of the aforementioned anode-side passivation layer [25], a cathode-side passivation layer can be simultaneously formed during the antisolvent process used to crystallize the $MAPbI_3$ layer [26]. Even without an additional coating process, issues related to the grain boundary and the problem of defects at the interface between the perovskite light-absorbing layer and ETL can be solved to realize highly efficient perovskite photodiodes. Additionally, dark and/or noise currents, which directly affect the responsivity and specific detectivity of photodetectors, can also be controlled by the cathode-side passivation layer. Thus, it is crucial to select proper interface engineering techniques for the perovskite light-absorbing layer, as doing so can improve the photocurrent and reduce the leakage and/or noise currents.

Herein, a high-performance self-powered $MAPbI_3$ perovskite photodiode with a cathode-side passivation layer of PMMA was systematically investigated. To assess the optoelectronic characteristics, we studied the responsivity, detectivity, and linear dynamic response range of $MAPbI_3$ perovskite photodiodes under a self-powered condition. Along with these observations, we measured the response times (rise/decay times) and stability characteristics of the photodiodes. Furthermore, we evaluated the device characteristics of the reference perovskite photodiodes without a PMMA passivation layer to support our results. The obtained results highlight the superior device performance of the perovskite photodetector with cathode-side PMMA passivation compared to a conventional reference device as well as previous perovskite photodetectors that rely on anode-side PMMA passivation.

2. Materials and Methods

2.1. Materials

Nickel(II) nitrate hexahydrate ($Ni(NO_3)_2 \cdot 6H_2O$, 99.999%), anhydrous dimethyl sulfoxide ($(CH_3)_2SO$, DMSO, 99.9%), *N*,*N*-dimethylformamide ($HCON(CH_3)_2$, DMF, 99.8%), anhydrous mono chlorobenzene (C_6H_5Cl, CB, 99.8%), and anhydrous isopropyl alcohol ($(CH_3)_2CHOH$, IPA, 99.7%) were purchased from Sigma-Aldrich Korea (Seoul, Republic of Korea) PMMA ($(C_5O_2H_8)_n$, 950,000 M_w) was purchased from Kayaku Advanced Materials (Westborough, MA, USA). Methyl ammonium iodide (CH_3NH_3I, MAI) and lead(II) iodide (PbI_2, 99.9985%) for the perovskite precursor were purchased from Greatcell Solar (Queanbeyan, NSW, Australia) and Alfa Aesar (Haverhill, MA, USA), respectively. Ethylene glycol ($HO(CH_2)_2OH$, EG, 99%) and IPA for the nickel oxide (NiO_x) precursor were purchased from Daejung Chemicals and Metals (Siheung, Republic of Korea). Phenyl-C61-buthyric acid methyl ester ($C_{72}H_{14}O_2$, $PCBM_{60}$) was purchased from Nano-C (Westwood, MA, USA). Bathocuproine ($C_{26}H_{20}N_2$, BCP, 98%) and a colloidal suspension of ZnO nanoparticles were procured from Tokyo Chemical Industry Co. Ltd. (Tokyo, Japan) and Nanograde (Zurich, Switzerland), respectively. All materials were used as received without further purification.

2.2. Methods

Pre-patterned 80-nm-thick indium tin oxide (ITO, 20 Ω/sq) layers on glass substrates were used as transparent anodes for the photodiodes. The ITO substrates used here were ultrasonically cleaned with ethanol, a detergent, and deionized (DI) water, after which they underwent an ultraviolet ozone treatment in an oven for 10 min.

For the NiO_x HTL, a precursor solution with 29 mg of $Ni(NO_3)_2 \cdot 6H_2O$ dissolved in mixed solvents of EG and IPA at a 6:4 volume ratio was prepared by stirring for 3 h. The precursor solution was then spin-coated onto the ITO substrate at 2600 rpm for 40 s, followed by 60 min of annealing at 300 °C to form the a 10-nm-thick NiO_x HTL. Subsequently, the substrates coated with the NiO_x layer were placed in a nitrogen-filled glovebox.

To fabricate the perovskite light-absorbing active layers of $MAPbI_3$, an antisolvent-assisted spin-coating method was used [25,26]. The perovskite precursor solution was prepared by dissolving PbI_2 and MAI at a 1:1 molar ratio in a mixed polar solvent of DMF and DMSO at an 8:2 volume ratio, with the precursor solution then stirred overnight. In the nitrogen-filled glovebox, the precursor solution was spin-coated onto the NiO_x-coated substrate at 4400 rpm for 30 s. During the spinning process, anhydrous CB or CB containing 0.05 wt% of PMMA was dropped onto the perovskite precursor-coated substrate as an antisolvent at a dripping delay time of 5–8 s after the spinning process had started. When the dripping time was changed from 5–8 s, the film quality of the fabricated perovskite layer was degraded and the film became inhomogeneous and hazy. Hence, in this study, we set the dripping time to 5–8 s to fabricate a uniform and homogeneous perovskite precursor layer without or with a cathode-side PMMA passivation layer. The perovskite precursor layer was then dried at room temperature for 5 min and subsequently annealed at 100 °C for 20 min to crystallize the $MAPbI_3$. The thicknesses of the $MAPbI_3$ layers studied here were nearly identical to each other (~250 nm), and the thickness of the PMMA layer was estimated to be less than 5 nm.

Thereafter, $PCBM_{60}$ in CB and a colloidal suspension of ZnO nanoparticles were subsequently spin-coated above the coated layers, resulting in a uniform 50-nm-thick $PCBM_{60}$ layer and a 20-nm-thick layer of ZnO as ETLs. The substrates were then transferred to a vacuum chamber for thermal evaporation of the 12-nm-thick BCP layer and 70-nm-thick Al cathode layer, subsequently at a base pressure below 2.0×10^{-6} torr. Thus, a photodiode with the structure of [ITO/NiO_x/$MAPbI_3$/PMMA/$PCBM_{60}$/ZnO/BCP/Al] was fabricated. All fabricated photodiodes had an active area of 6 mm^2.

2.3. Characterization

The surface morphology of the $MAPbI_3$ perovskite layer was analyzed with a scanning electron microscope (Inspect F50, FEI Company, Hillsboro, OR, USA). ImageJ software (National Institutes of Health, Bethesda, MD, USA) was used to analyze the grain size distributions in the $MAPbI_3$ perovskite layers from the observed SEM images.

The UV–Visible optical adsorption spectra were studied using an UV–Vis spectrometer (Agilent 8453 Diode Array UV-VIS, Agilent Technologies, Inc., Santa Clara, CA, USA). The contact angles of the fabricated $MAPbI_3$ films were measured with a contact angle goniometer (Ossila, London, UK).

A monochromatic light source of a 637 nm diode laser (model COMPACT-100G-637-A, 100 mW, maximum internal modulation frequency: 50 kHz, World Star Tech, Markham, OT, Canada) was used to assess the performance of the photodetector. Keithley source meters (models 2400 and 2636, Tektronix, Inc. Beaverton, OR, USA) were used to assess the current-versus-voltage (*J*–*V*) characteristics. An incident photon-to-current conversion efficiency (IPCE) measurement system (ORIEL IQE-200, Newport, Irvine, CA, USA) was used to measure the spectral responsivity, R(λ), of the photodiode.

The noise current levels of the photodiode were obtained from the fast Fourier transform of the measured dark currents of the photodiode as a function of time using the 2636 Keithley source meter operated at a sampling rate of 1 kHz. The 3 dB cutoff bandwidths of the photodiodes were estimated from the logarithmic transform of their normal-

ized photo responses, measured as a function of the modulation frequency of the irradiated light using the 637 nm laser system.

3. Results

3.1. Characteristics of $MAPbI_3$ Layers with a PMMA Passivation Layer

A schematic illustration of the passivation layer of the PMMA on a $MAPbI_3$ perovskite layer is shown in Figure 1a. As illustrated in the figure, PMMA dissolved in an antisolvent can simply be spin-coated during the formation of a 250-nm-thick $MAPbI_3$ perovskite light-absorbing layer. To verify the formation of the PMMA passivation layer on the perovskite layer, first, we observed the contact angles of DI water on the fabricated films (Figure 1b). As shown in the figure, the water contact angle on the $NiO_x/MAPbI_3$/PMMA perovskite film (sample) was 37.4°, significantly higher than that (~26.8°) of the $NiO_x/MAPbI_3$ perovskite film (reference). This increase in the water contact angle mainly stems from the intrinsic hydrophobicity of the PMMA layer in the sample film, providing evidence of the simple and reliable fabrication method of the PMMA passivation layer on the perovskite layer. Thus, such a hydrophobic PMMA passivation layer may affect the growth of the grains of the underlying $MAPbI_3$ perovskite by tailoring the nucleation of the perovskite crystal growth [3,13,27]. It is noteworthy that the coated PMMA polymers mainly existed at the perovskite/ETL interface, with some of the polymer possibly present inside the perovskite layer, similar to an earlier conjugated polymer that formed an interfacial passivation layer [20].

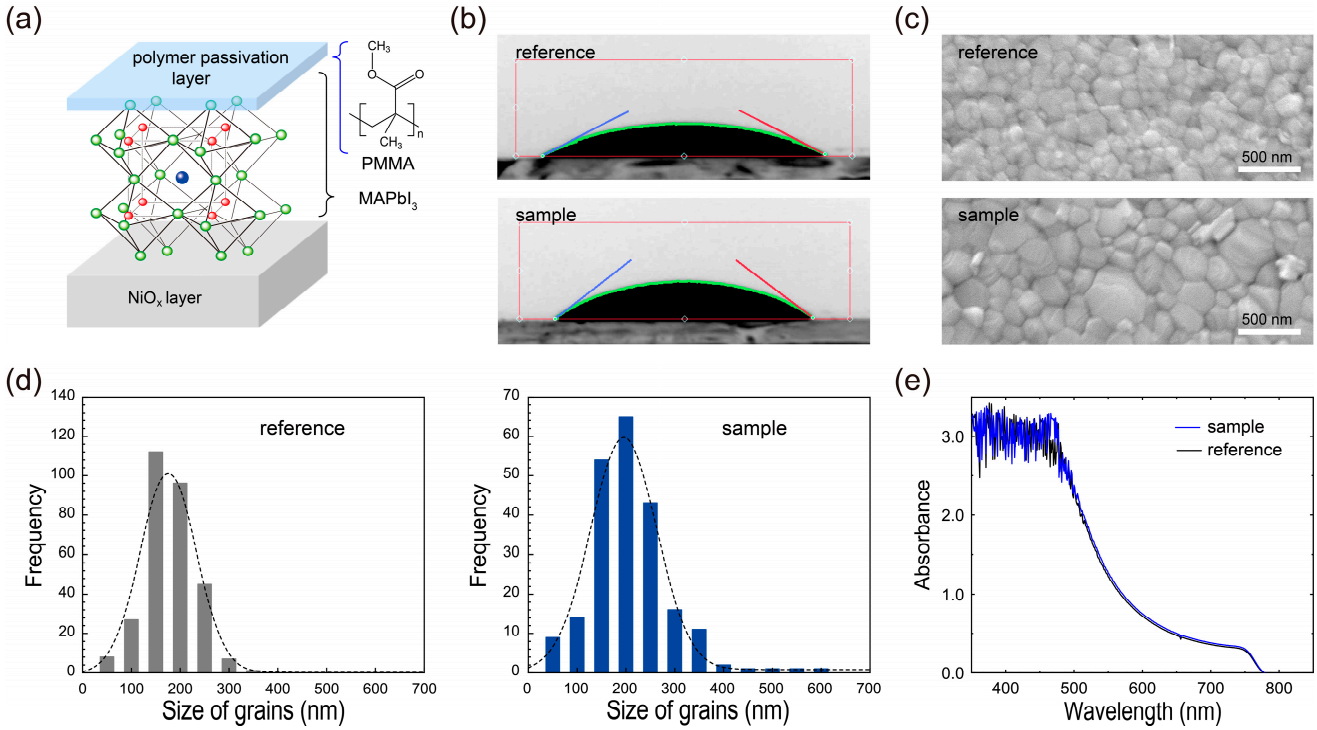

Figure 1. (**a**) Schematic illustration of the polymer passivation layer of PMMA on a $MAPbI_3$ perovskite layer and corresponding chemical structure. (**b**) Comparisons of the water contact angles on the $NiO_x/MAPbI_3$ perovskite (reference) and $NiO_x/MAPbI_3$ perovskite/PMMA (sample) layers, corresponding to (**c**) high-magnification top-view SEM images and (**d**) grain size distributions derived from the SEM images. (**e**) UV–Visible optical absorption spectra of the reference and sample layers.

To assess the effect of the PMMA passivation layer on the growth of grains for the $MAPbI_3$ perovskite films, scanning electron microscopy (SEM) was utilized. The surface morphologies obtained from the SEM observations are shown in Figure 1c. As shown in these SEM images, the surfaces of both perovskite films were fairly smooth and showed well-packaged grains. However, compared to the reference film without a passivation layer,

it is clear that the introduction of the PMMA layer affected the increment of the grain size while also decreasing the number of grain sites in the sample perovskite film.

For an additional quantitative analysis, ImageJ software was used to adjust the contrast of the SEM images of the $MAPbI_3$ perovskite layers without/with a PMMA passivation layer (Figure 1c) and to identify the borders of the grains in the SEM images. Then, utilizing the black and white threshold of each adjusted SEM image, it was possible to estimate the range of the domain sizes of the surrounding grains. Histograms of the domain size distributions for $MAPbI_3$ perovskite layers without/with a PMMA passivation layer are presented in Figure 1d. As shown in this figure, the average grain size of the reference film was ~151 nm, while that of the sample film was ~196 nm, clearly demonstrating that the average grain size of the $MAPbI_3$ layer was increased significantly due to the presence of the PMMA passivation layer. From these SEM studies, it was confirmed that the generation of unnecessary $MAPbI_3$ nucleation could be significantly suppressed by the coordinate bonding of the carbonyl of the PMMA polymer with the uncoordinated Pb ions of $MAPbI_3$ [28–30]. Thus, the PMMA passivation layer enables an increase in the $MAPbI_3$ grain size while also mitigating film defects such as spikes and/or pinholes [31,32].

Apart from the increased grain size of the $MAPbI_3$ perovskite layer, the PMMA passivation layer can effectively cover defects and grain boundaries in the perovskite layer, possibly providing an effective passivation route for interface defects between the $MAPbI_3$ layer and the adjacent ETL [33,34]. Moreover, due to the improved interface quality of the $MAPbI_3$ layer stemming from the PMMA, the reduction in the recombination loss of charge carriers can improve the charge carrier extraction from the $MAPbI_3$ layer to the charge transport layers [31,32,34–36]. Thus, given these properties of the $MAPbI_3$ layer in the sample films, we hold that the introduction of a PMMA passivation layer can effectively improve the film and interface qualities of the $MAPbI_3$ layer, likely leading to an improvement in the optoelectronic performance of perovskite devices, even without any critical changes in the optical characteristics such as the optical absorption capabilities (Figure 1e) [25]. To confirm this, the optical absorption characteristics of the reference and sample perovskite films were also investigated, as shown in Figure 1e. In this figure, strong absorption in the visible range of 450~700 nm for the reference and sample films could be observed. Notably, the sample film showed an optical absorption nearly identical to that of the reference perovskite film, proving that the PMMA passivation layer did not significantly change or deteriorate the optical absorption properties of the perovskite layer. Thus, by introducing the PMMA passivation layer onto the perovskite layer, modification of the interface between the $MAPbI_3$ layer and the ETL can be anticipated.

3.2. Characterization of Perovskite Photodiodes without and with a PMMA Passivation Layer

Inspired by the desirable passivation effect of PMMA described above, we fabricated $MAPbI_3$ photodiodes with the device structure illustrated in Figure 2a. As shown in the figure, ITO acts as a transparent anode, with NiO_x used as a HTL, $MAPbI_3$ as a perovskite light-absorbing layer, and PMMA as the cathode-side passivation layer. $PCBM_{60}$, ZnO nanoparticles and BCP were utilized as the ETLs and Al was used as the top cathode electrode.

To evaluate the device performance of the fabricated $MAPbI_3$ photodiodes without (reference) and with a PMMA passivation layer (sample), the dark-current densities (J_{dark}) were investigated as a function of the applied voltage (J_{dark}-V). As indicated in Figure 2b, excellent diode characteristics with large rectifying ratios (*RR*s) and low leakage current densities were found in these photodiodes. Due to the suppression of the leakage currents by the PMMA passivation layer, a somewhat higher *RR* value, 6.1×10^5 (at 1.0 V), for the sample was obtained compared to that (5.3×10^5) of the reference, indicative of the useful film properties of the $MAPbI_3$ perovskite films, as above-mentioned. It is also noteworthy that the observed *RR* values were one order higher than the corresponding values in the literature [13]. Similarly, the PMMA passivation layer in the sample led to a reduced average J_{dark} value of 5.1×10^{-7} mA/cm^2 at zero applied voltage, lower than that (7.3×10^{-7} mA/cm^2) of the reference without a PMMA layer, providing evidence of the

suppressed leakage currents caused by the improved interfacial quality of the perovskite light-absorbing layer.

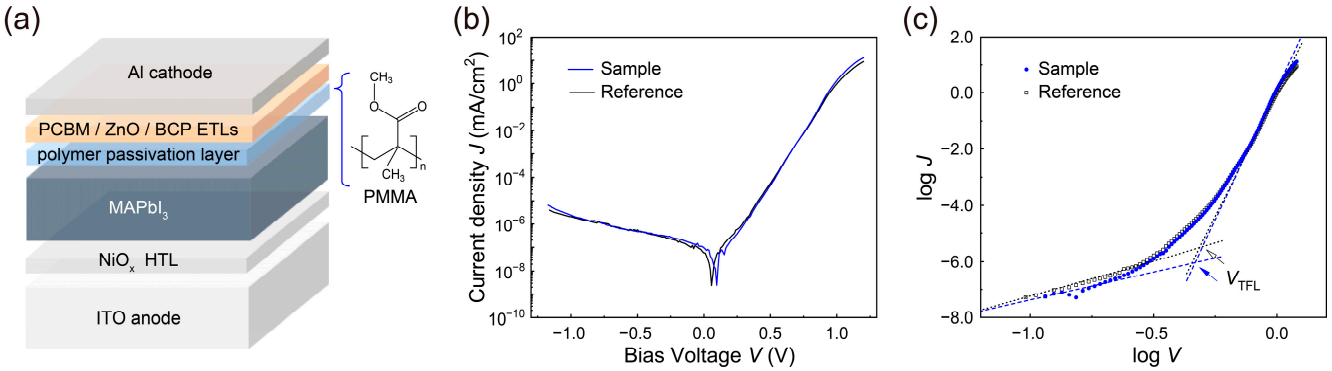

Figure 2. (**a**) Schematic device configuration of a $MAPbI_3$ photodiode with a cathode-side PMMA passivation layer. Dark-current density-voltage (J_{dark}-V) characteristics of $MAPbI_3$ photodiodes without (reference) and with a cathode-side PMMA passivation layer (sample) on (**b**) a semi-log scale and (**c**) a log–log scale.

Furthermore, for an in-depth examination of the perovskite photodiodes presented here, their trap-filled limit voltages (V_{TFL}s) were estimated from the J_{dark}–V curves on a log–log scale (Figure 2c) [13,20,32,37,38]. The obtained V_{TFL} values for the reference and sample were ~0.49 and 0.47 V, respectively. Based on the V_{TFL} values, the trap density states (n_{trap}) can also be estimated using the space–charge–limited current model, as follows [38,39]:

$$V_{TFL} = \frac{qn_{trap}L^2}{2\varepsilon_0\varepsilon_p} \quad (1)$$

In this equation, q is the elementary charge, L is the thickness of the perovskite layer, while ε_0 and ε_p are the dielectric constants of the vacuum and perovskite, respectively. The estimated n_{trap} values were around 1.30×10^{15} cm^{-3} for the reference and 1.25×10^{15} cm^{-3} for the sample, indicating that the PMMA layer in the sample could effectively passivate defects at the interface between the perovskite layer and the ETL.

Subsequently, we measured the photocurrents as a function of the bias voltage in the range of ±1.2 V (I_{light} -V) for several input power levels (Ps) of incident laser light with a wavelength of λ = 637 nm, as shown in Figure 3a. In the figure, the open-circuit potential (V_{OC}) and the short-circuit current (I_{SC}) increased considerably as the input power of the incident light was increased. For a detailed comparison, the built-in potentials (V_{bi}s) of the reference and sample were obtained using the Shockley diode model equation, expressed as follows,

$$V_{bi} = -\left(\frac{nk_BT}{e}\right)\ln J_0, \quad (2)$$

where k_B is the Boltzmann's constant; T is the temperature; n is the ideality factor; and J_0 is the reverse-saturated current density [13,40–42]. The estimated values of V_{bi} and n were approximately 0.58 V and 1.49, respectively, for the sample, slightly higher than the V_{bi} value of approximately 0.57 V and the n value of about 1.47 for the reference. As the thickness of the PMMA layer was considered to be less than ~5 nm, it is clear that the PMMA passivation layer did not degrade the built-in potential despite its intrinsic insulating properties. It should be noted that the short-circuit current I_{SC} and built-in potential V_{bi} began to decrease noticeably as the thickness of each functional layer, especially the PMMA layer or the $MAPbI_3$ layer, was changed from its optimized thickness.

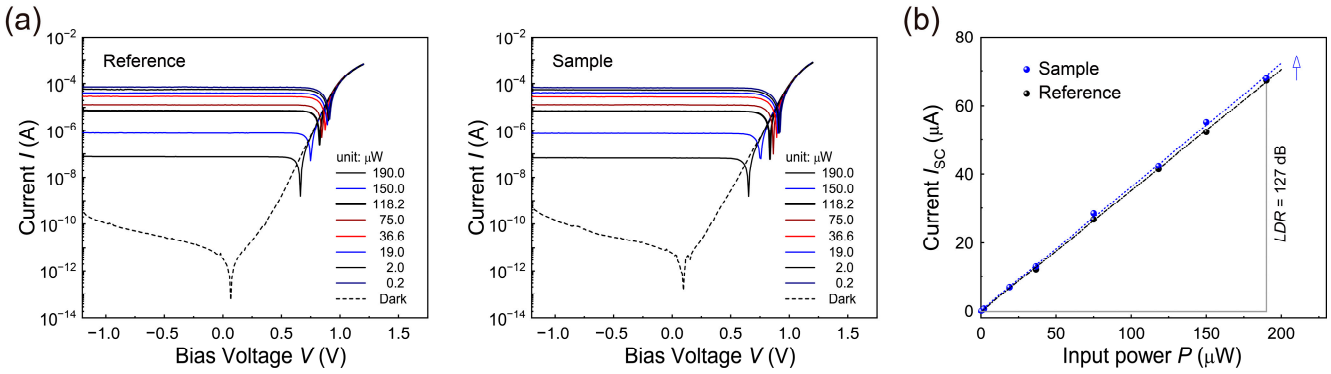

Figure 3. (**a**) Photocurrent characteristics of the $MAPbI_3$ photodiodes of the reference (**left**) and sample (**right**) as a function of the bias voltage for several different intensity levels of irradiating light with a wavelength of 637 nm. (**b**) I_{SC} curves as a function of the input power of incident light (637 nm) for the reference and sample photodiodes.

Next, the I_{SC} values of the reference and sample were determined using Figure 3a and are plotted as a function of the input power of the incident laser light (Figure 3b). It is clear from the figure that even under the self-powered condition (at zero bias voltage), large numbers of charge carriers become separated by the built-in potential, resulting in a considerable increment of I_{SC}. With the power law of

$$I_{SC} = \kappa \times P^{\theta}, \tag{3}$$

where κ is a proportional constant and θ is the power law index, the trap states existing in the $MAPbI_3$ perovskite light-absorbing layer studied here can be analyzed [13,20,43]. We obtained θ values for both the reference and sample using the power law above with the best fitted parameter values, determining an θ value of 0.999 for the sample, which is much closer to θ = 1.0 for an ideal photodiode compared to the value of θ = 0.984 for the reference without a PMMA layer. Hence, the cathode-side PMMA passivation layer can effectively decrease the number of trap states and reduce the second-order recombination loss under a short-circuit condition (i.e., self-powered condition).

Next, based on the photocurrent data in Figure 3b, the responsivity at the wavelength of λ (R_λ) for the reference and sample were estimated using the equation.

$$R_\lambda = \left(\frac{I_{PH}}{P}\right) \text{ and } I_{PH} = I_{light} - I_{dark} \tag{4}$$

where I_{PH} denotes the net photocurrent [7,9,12–14,20]. The responsivity R_{637} value at the wavelength λ = 637 nm of incident light under zero bias voltage as obtained here was approximated as 360 mA/W for the sample with the PMMA passivation layer, higher than that (~352 mA/W) of the reference at zero bias voltage.

To evaluate the photodiode performance over a wide light intensity range, we also calculated the linear dynamic range (*LDR*) of the photodiodes using the equation [7,9,12,14,20]:

$$LDR = 20 \log\left(\frac{I_{PH}}{I_{dark}}\right) \tag{5}$$

Even at zero bias voltage, a notably higher *LDR* value was realized, ~127 dB, for the sample compared to that (~124 dB) of the reference. These high values of R_λ and *LDR* are clear evidence of the excellent photoelectric conversion ability and remarkably good linearity over a wide range of incident light intensity for the sample with the cathode-side PMMA passivation layer. It should also be noted that the sample device showed a relatively high *LDR* value compared to those of previous perovskite thin-film photodetectors and industrial silicon photodetectors (90~120 dB). Given the nearly ideal value of θ and the

high values of R_λ and *LDR*, the cathode-side PMMA passivation layer can serve to realize trap-less perovskite photodiodes.

For a further evaluation of the photodiode performance, the R_λ spectra were also measured using an IPCE system in the self-powered condition, as presented in Figure 4a. This figure indicates that the peak R_λ value of ~401 mA/W for the sample was notably higher than that (386 mA/W) for the reference and higher than those of the $MAPbI_3$-based photodiodes in the literature [9,13,25]. This finding clearly shows that the improved interface of the $MAPbI_3$ layer for efficient charge extraction is crucial when attempting to realize high responsivity from perovskite photodiodes.

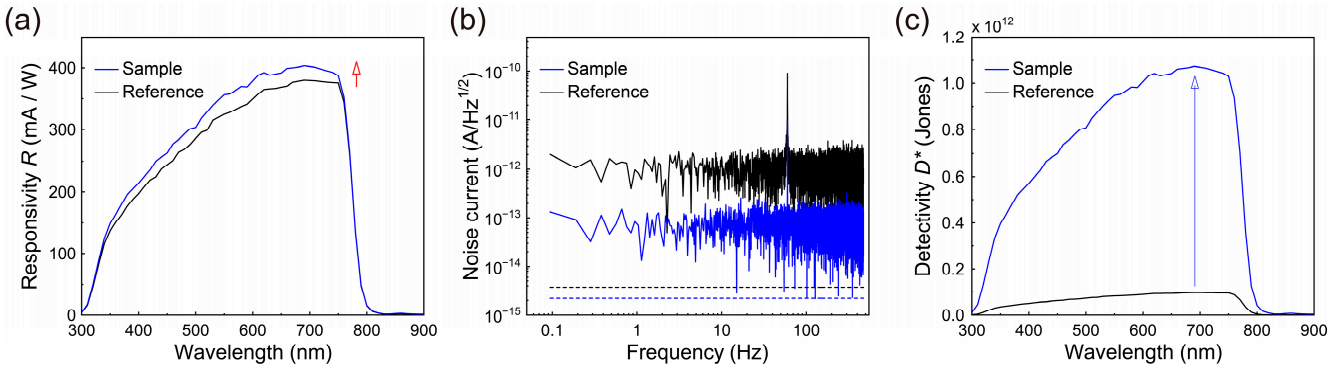

Figure 4. (**a**) Responsivity R_λ spectra at zero bias voltage, (**b**) noise currents vs. frequency characteristics, and (**c**) specific detectivity D^* spectra at zero bias voltage for the photodiodes of the reference and sample. The dotted lines in (**b**) show the shot noise levels for the reference (black) and sample (blue).

Subsequently, we analyzed the noise current (i_n) of the photodiodes. At an ambient temperature, the dark currents (I_{dark}) were measured over time with no voltage applied. Subsequently, the dark currents were fast Fourier transformed and plotted as a function of the frequency, as shown in Figure 4b [7,10,11,20,44], where the photodiodes exhibited white noise unrelated to the frequency in the ranges observed here. Additionally, as shown in the figure, the noise level of each photodiode was evaluated at a bandwidth of 1 Hz. The estimated noise level of the sample was ~0.09 pA $Hz^{-1/2}$ at a bandwidth of 1 Hz, somewhat lower than that (0.96 pA $Hz^{-1/2}$) of the reference. This indicates that the proposed cathode-side PMMA passivation layer clearly suppresses the noise level by passivating unwanted film defects at the interface between the $MAPbI_3$ layer and the $PCBM_{60}$ ETL.

Next, the obtained values of i_n and R_λ were applied to assess the noise equivalent power (*NEP*) in an effort to determine the minimum detectable incident optical power using the relationship of [7,9,11,12,14,45,46]:

$$NEP = \frac{i_n}{R_\lambda} \tag{6}$$

The obtained minimum *NEP* value for the sample was ~230 fW/$Hz^{1/2}$, notably less than that (~2520 fW/$Hz^{1/2}$) for the reference at zero bias voltage. This clearly indicates that the cathode-side PMMA passivation layer can enhance the low-power-detection ability of the $MAPbI_3$ photodiode compared to a non-passivated $MAPbI_3$ photodiode.

Based on the *NEP* values presented above, the specific detectivity D^* values of the photodiodes were also evaluated under the self-powered condition in order to evaluate their weak-signal detection capacities. This was carried out with the following equation,

$$D^* = \frac{\sqrt{A \cdot B}}{NEP}, \tag{7}$$

where A and B are the active area of the device and the 1 Hz specific bandwidth, respectively [7,9–14,20,44–49]. In the self-powered condition, the estimated specific detectivity D^* spectra for the reference and sample using Equation (7) are plotted in Figure 4c. As shown

in this figure, while the peak value of D^* was ~0.97 × 10^{11} Jones for the reference, the peak value of D^* for the sample was ~1.07 × 10^{12} Jones, which is more than eleven times greater for weak-signal detection compared to the reference. Hence, the suppression of unnecessary leakage/noise currents by the cathode-side PMMA passivation layer clearly increased the photodetector performance outcomes. Additionally, the D^* value of 1.07 × 10^{12} Jones for the sample was conspicuously higher than those (D^* value ~0.81 × 10^{12} Jones) of the $MAPbI_3$ photodiodes in the literature with an anode-side PMMA passivation layer at the interface between the $MAPbI_3$ perovskite light-absorbing layer and the NiO_x HTL; this was also comparable to those of commercial silicon photodetectors [14,20,25,47].

As another comparison, we also estimated the conventional simplified specific detectivity D^* values of the reference and sample based on the shot noise ($i_{n,s}$), as estimated from the dark-current density (J_{dark}) with the simple relationship of $D^* \sim R_\lambda / \sqrt{2eJ_{dark}}$ [7,9,13,14,48,49]. The estimated peak value of the simplified D^* for the reference was ~2.5 × 10^{13} Jones. In contrast, the peak value of simplified D^* for the sample showed an increase to ~4.5 × 10^{13} Jones. It should also be noted that the simplified D^* value for the sample was significantly higher compared to earlier values for other $MAPbI_3$ thin-film-based photodiodes previously reported in the literature [25,48,49]. However, such simplified D^* values may be overestimated because the shot noise levels were lower than their measured noise current values, as indicated by the dotted lines in Figure 4b [49].

To assess the dynamic characteristics of the photodiodes studied here, the temporal responses were investigated at zero bias voltage by irradiating monochromatic light (λ = 637 nm, P = 190 μW) modulated at a frequency of 2 kHz (Figure 5a). In Figure 5a, the measured temporal responses of the sample clearly indicated higher photocurrents than those of the reference, as expected. The response times of the rise (τ_r) and decay (τ_d) times were determined as the time intervals required to change the photocurrent signal amplitudes between 10% (I_{10}) and 90% (I_{90}) up the rising and decay edges of the signal curves, respectively; τ_r and τ_d for the sample were ~50 and ~17 μs, respectively, similar to those (~49 and ~18 μs) of the reference. Moreover, the obtained response times for the sample and reference were considerably shorter than those of $MAPbI_3$-based photodiodes in the literature [13].

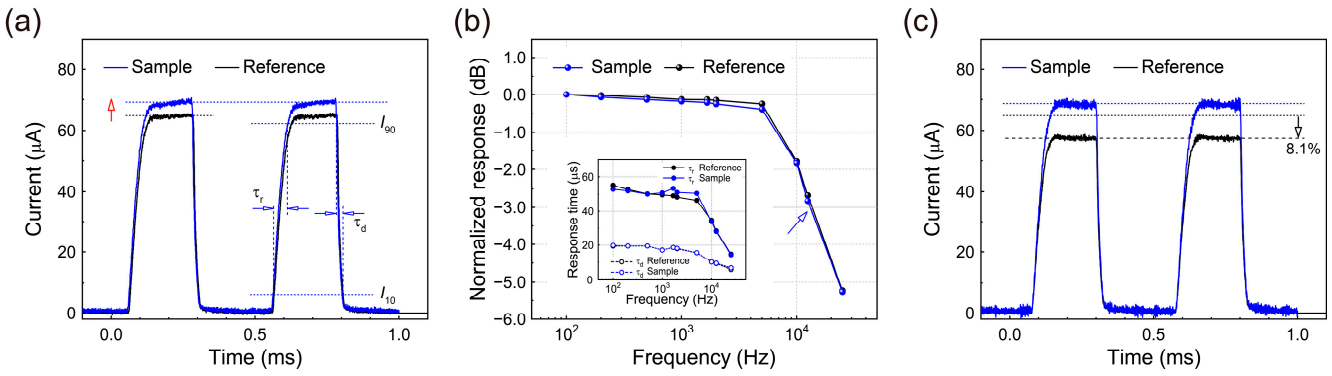

Figure 5. (**a**) Temporal photo responses of the reference and sample $MAPbI_3$ photodiodes at zero bias voltage when turning the incident light (λ = 637 nm, P = 190 μW) on and off (2 kHz). The rise (τ_r) and decay (τ_d) times were determined as the time intervals between the 10% (I_{10}) and 90% (I_{90}) amplitude levels of the signal, respectively. (**b**) Normalized photocurrent versus the modulation frequency of incident light (p = 190 μW, 637 nm). The inset shows the dependences of τ_r and τ_d on the modulation frequency for the photodiodes studied here. (**c**) Temporal photo responses of the reference and sample photodiodes when stored for 500 h.

Next, the 3 dB cutoff bandwidths (f_{-3dB}) for the photodiodes were measured. These values were f_{-3dB} = ~1.40 × 10^4 and ~1.33 × 10^4 Hz for the reference and sample, respectively (Figure 5b). These dynamic photo responses of the photodiodes indicate that the limitation of the response bandwidths in the devices may stem mainly from the *RC* time constants of the devices, implying that additional improvements in the response speed

can be achieved by greater optimization of the device architecture [45]. Additionally, it should be noted that as the modulation frequency applied to the irradiated laser light was increased, the observed rise and decay times began to decrease continuously in the frequency range investigated here, as shown in the inset of Figure 5b.

Finally, we investigated another important functionality of the PMMA passivation layer based on its excellent hydrophobicity, as shown in Figure 1b. Herein, the storage stability of the photodiodes was measured in terms of the photocurrent flowing through the photodiode devices. Given that the storage lifetime is closely linked to water permeation into the functional layers, particularly the $MAPbI_3$ active layer, measuring the temporal responses of the stored photodiodes can provide information pertaining to the degradation mechanisms in these devices [50].

To measure the storage stability, the devices in this study were stored in a nitrogen glovebox between successive measurements of their temporal responses at a regular time interval of approximately 48 h. Temporal response measurements were also taken at zero bias at room temperature. Figure 5c presents the representative temporal response characteristics for the photodiodes stored for a total storage time of ~500 h. As shown in the figure, the photocurrent of the reference was reduced significantly to ~91.9% of its original value after being stored for approximately 500 h. In contrast, the sample exhibited a relatively negligible decrement (~0%) of the photo-response, even after the long storage time used here. Thus, as clearly shown in the figure, the sample with the cathode-side PMMA passivation layer is much more stable than the reference without a PMMA layer, indicating once again that the PMMA passivation layer significantly enhances the storage stability of $MAPbI_3$ perovskite photodiodes. Additional details related to the long-term and/or continuous stability of the photodiode with the PMMA passivation layer, together with a more stable Ag, Cu, or Au cathode instead of the Al cathode used here, will be discussed elsewhere.

4. Discussion

The observations above highlight the effects of the cathode-side PMMA passivation layer; it not only improved the quality of the film but also decreased the leakage/noise currents through the $MAPbI_3$ perovskite layers, thus providing a new paradigm of a high, fast, and durable performance of $MAPbI_3$ perovskite-based photodiodes. Additional developments of organic/inorganic perovskite layers and/or the introduction of other novel functional layers will result in further improvements in the device performance for self-powered, highly sensitive, and stable solution-processable perovskite photodiodes with a cathode-side PMMA passivation layer.

5. Conclusions

In this study, we demonstrated that the introduction of a cathode-side PMMA passivation layer between an absorber layer of $MAPbI_3$ and the ETL effectively suppressed the leakage/noise currents and in turn improved the performance of the self-powered solution-processable $MAPbI_3$ photodiodes. With the cathode-side PMMA passivation layer, the interface quality of the $MAPbI_3$ perovskite layer was shown to be improved, and the film defects were reduced. Moreover, we noted an increase in the grain size and effective decrements in the recombination losses as well as the noise currents. Consequently, even at zero bias voltage, the $MAPbI_3$ photodiode with the PMMA passivation layer exhibited a notably high specific detectivity D^* of ~1.07×10^{12} Jones. Moreover, a significantly low *NEP* of ~230 $fW/Hz^{1/2}$ and wide *LDR* of ~127 dB were achieved. The $MAPbI_3$ photodiode with the PMMA passivation layer revealed excellent device performance compared to that of a conventional $MAPbI_3$ photodetector without a passivation layer. A rapid rise response time of 50 μs and decay response times of 17 μs were also obtained, as were highly durable dynamic responses of the photodiode, even after a long storage time of nearly 500 h. These findings provide clear evidence of the remarkably improved device performance of a perovskite photodiode with a noise-reducing PMMA passivation layer

at the interface between the $MAPbI_3$ perovskite light-absorbing layer and the ETL. Thus, a cathode-side PMMA passivation layer in a perovskite photodiode, as presented here, can enhance the applicability of interface-engineered perovskites in photodiodes, imaging sensors, and various low-energy-consuming light-detecting devices.

Author Contributions: Conceptualization, W.K. and Y.A.; Data curation, W.K., J.P. and S.S.; Formal analysis, W.K., J.P. and S.S.; Methodology, J.P.; Project administration, E.H.C. and B.P.; Writing—original draft, W.K. and Y.A.; Writing—review & editing, J.P., E.H.C. and B.P. All authors have read and agreed to the published version of the manuscript.

Funding: This research was funded by the National Research Foundation of Korea (2020R1A2B5B03097060, 2021R1A6A1A03038785) and by Kwangwoon University (2022).

Institutional Review Board Statement: Not applicable.

Informed Consent Statement: Not applicable.

Data Availability Statement: Data presented in this study are available on request from the corresponding author.

Conflicts of Interest: The authors declare no conflict of interest.

References

1. Kojima, A.; Teshima, K.; Shirai, Y.; Miyasaka, T. Organometal Halide Perovskites as Visible-Light Sensitizers for Photovoltaic Cells. *J. Am. Chem. Soc.* **2009**, *131*, 6050–6051. [CrossRef] [PubMed]
2. Lee, M.M.; Teuscher, J.; Miyasaka, T.; Murakami, T.N.; Snaith, H.J. Efficient Hybrid Solar Cells based on Meso-Superstructured Organometal Halide Perovskites. *Science* **2012**, *338*, 643–647. [CrossRef] [PubMed]
3. Bi, C.; Wang, Q.; Shao, Y.; Yuan, Y.; Xiao, Z.; Huang, J. Non-wetting Surface-Driven High-Aspect-Ratio Crystalline Grain Growth for Efficient Hybrid Perovskite Solar Cells. *Nat. Commun.* **2015**, *6*, 7747. [CrossRef] [PubMed]
4. Momblona, C.; Gil-Escrig, L.; Bandiello, E.; Hutter, E.M.; Sessolo, M.; Lederer, K.; Blochwitz-Nimoth, J.; Bolink, H.J. Efficient Vacuum Deposited p-i-n and n-i-p Perovskite Solar Cells Employing Doped Charge Transport Layers. *Energy Environ. Sci.* **2016**, *9*, 3456–3463. [CrossRef]
5. Eperon, G.E.; Leijtens, T.; Bush, K.A.; Prasanna, R.; Green, T.; Wang, J.T.-W.; McMeekin, D.P.; Volonakis, G.; Milot, R.L.; May, R.; et al. Perovskite-Perovskite Tandem Photovoltaics with Optimized Bandgaps. *Science* **2016**, *354*, 861–865. [CrossRef]
6. Yang, W.S.; Park, B.-W.; Jung, E.H.; Jeon, N.J.; Kim, Y.C.; Lee, D.U.; Shin, S.S.; Seo, J.; Kim, E.K.; Noh, J.H.; et al. Iodide management in formamidinium-lead-halide-based perovskite layers for efficient solar cells. *Science* **2017**, *356*, 1376–1379. [CrossRef]
7. Dou, L.; Yang, Y.M.; You, J.; Hong, Z.; Chang, W.-H.; Li, G.; Yang, Y. Solution-Processed Hybrid Perovskite Photodetectors with High Detectivity. *Nat. Commun.* **2014**, *5*, 5404. [CrossRef]
8. Kwon, K.C.; Hong, K.; Van Le, Q.; Lee, S.Y.; Choi, J.; Kim, K.-B.; Kim, S.Y.; Jang, H.W. Inhibition of Ion Migration for Reliable Operation of Organolead Halide Perovskite-Based Metal/Semiconductor/Metal Broadband Photodetectors. *Adv. Funct. Mater.* **2016**, *26*, 4213–4222. [CrossRef]
9. Veeramalai, C.P.; Feng, S.; Zhang, X.; Pammi, S.V.N.; Pecunia, V.; Li, C. Lead–halide Perovskites for Next-Generation Self-Powered Photodetectors: A Comprehensive Review. *Photonics Res.* **2021**, *9*, 968–991. [CrossRef]
10. Shen, L.; Fang, Y.; Wang, D.; Bai, Y.; Deng, Y.; Wang, M.; Lu, Y.; Huang, J. A Self-Powered, Sub-nanosecond-Response Solution-Processed Hybrid Perovskite Photodetector for Time-Resolved Photoluminescence-Lifetime Detection. *Adv. Mater.* **2016**, *28*, 10794–10800. [CrossRef]
11. Fang, Y.; Huang, J. Resolving Weak Light of Sub-picowatt per Square Centimeter by Hybrid Perovskite Photodetectors Enabled by Noise Reduction. *Adv. Mater.* **2015**, *27*, 2804–2810. [CrossRef]
12. Zhao, Y.; Li, C.; Shen, L. Recent Advances on Organic-Inorganic Hybrid Perovskite Photodetectors with Fast Response. *InfoMat* **2019**, *1*, 164–182. [CrossRef]
13. Afzal, A.M.; Bae, I.-G.; Aggarwal, Y.; Park, J.; Jeong, H.-R.; Choi, E.H.; Park, B. Highly Efficient Self-Powered Perovskite Photodiode with an Electron-Blocking Hole-Transport NiO_x Layer. *Sci. Rep.* **2021**, *11*, 169. [CrossRef]
14. Gong, X.; Tong, M.; Xia, Y.; Cai, W.; Moon, J.S.; Cao, Y.; Yu, G.; Shieh, C.-L.; Nilsson, B.; Heeger, A.J. High-Detectivity Polymer Photodetectors with Spectral Response from 300 nm to 1450 nm. *Science* **2009**, *325*, 1665–1667. [CrossRef]
15. Son, D.-Y.; Lee, J.-W.; Choi, Y.J.; Jang, I.-H.; Lee, S.; Yoo, P.J.; Shin, H.; Ahn, N.; Choi, M.; Kim, D.; et al. Self-Formed Grain Boundary Healing Layer for Highly Efficient $CH_3NH_3PbI_3$ Perovskite Solar Cells. *Nat. Energy* **2016**, *1*, 16081. [CrossRef]
16. Bi, D.; Tress, W.; Dar, M.I.; Gao, P.; Luo, J.; Renevier, C.; Schenk, K.; Abate, A.; Giordano, F.; Baena, J.-P.C.; et al. Efficient Luminescent Solar Cells based on Tailored Mixed-Cation Perovskites. *Sci. Adv.* **2016**, *2*, e1501170. [CrossRef]
17. Zheng, X.; Chen, B.; Dai, J.; Fang, Y.; Bai, Y.; Lin, Y.; Wei, H.; Zeng, X.C.; Huang, J. Defect Passivation in Hybrid Perovskite Solar Cells using Quaternary Ammonium Halide Anions and Cations. *Nat. Energy* **2017**, *2*, 17102. [CrossRef]

18. Aydin, E.; De Bastiani, M.; De Wolf, S. Defect and Contact Passivation for Perovskite Solar Cells. *Adv. Mater.* **2019**, *31*, 1900428. [CrossRef]
19. Cai, F.; Cai, J.; Yang, L.; Li, W.; Gurney, R.S.; Yi, H.; Iraqi, A.; Liu, D.; Wang, T. Molecular Engineering of Conjugated Polymers for Efficient Hole Transport and Defect Passivation in Perovskite Solar Cells. *Nano Energy* **2018**, *45*, 28–36. [CrossRef]
20. Wang, D.; Xu, W.; Min, L.; Tian, W.; Li, L. Interfacial Passivation and Energy Level Alignment Regulation for Self-Powered Perovskite Photodetectors with Enhanced Performance and Stability. *Adv. Mater. Interfaces* **2022**, *9*, 2101766. [CrossRef]
21. Wang, C.; Liu, M.; Rahman, S.; Pasanen, H.P.; Tian, J.; Li, J.; Deng, Z.; Zhang, H.; Vivo, P. Hydrogen Bonding Drives the self-Assembling of Carbazole-Based Hole-Transport Material for Enhanced Efficiency and Stability of Perovskite Solar Cells. *Nano Energy* **2022**, *101*, 107604. [CrossRef]
22. Li, R.; Liu, M.; Matta, S.K.; Hiltunen, A.; Deng, Z.; Wang, C.; Dai, Z.; Russo, S.P.; Vivo, P.; Zhang, H. Sulfonated Dopant-Free Hole-Transport Material Promotes Interfacial Charge Transfer Dynamics for Highly Stable Perovskite Solar Cells. *Adv. Sustain. Syst.* **2021**, *5*, 2100244. [CrossRef]
23. Piao, C.; Xi, J.; Choi, M. Directionally Selective Polyhalide Molecular Glue for Stable Inverted Perovskite Solar Cells. *Sol. RRL* **2020**, *4*, 2000244. [CrossRef]
24. Kim, M.; Motti, S.G.; Sorrentino, R.; Petrozza, A. Enhanced Solar Cell Stability by Hygroscopic Polymer Passivation of Metal Halide Perovskite Thin Film. *Energy Environ. Sci.* **2018**, *11*, 2609–2619. [CrossRef]
25. Park, J.; Aggarwal, Y.; Kim, W.; Sharma, S.; Choi, E.H.; Park, B. Self-powered $CH_3NH_3PbI_3$ Perovskite Photodiode with a Noise-Suppressible Passivation Layer of Poly(Methyl Methacrylate). *Opt. Express* **2023**, *31*, 1202–1213. [CrossRef]
26. Frolova, L.A.; Davlethanov, A.I.; Dremova, N.N.; Zhidkov, I.; Akbulatov, A.F.; Kurmaev, E.Z.; Aldoshin, S.M.; Stevenson, K.J.; Troshin, P.A. Efficient and Stable $MAPbI_3$-Based Perovskite Solar Cells using Polyvinylcarbazole Passivation. *J. Phys. Chem. Lett.* **2020**, *11*, 6772–6778. [CrossRef]
27. Du, Y.; Xin, C.; Huang, W.; Shi, B.; Ding, Y.; Wei, C.; Zhao, Y.; Li, Y.; Zhang, X. Polymeric Surface Modification of NiO_x-Based Inverted Planar Perovskite Solar Cells with Enhanced Performance. *ACS Sustain. Chem. Eng.* **2018**, *6*, 16806–16812. [CrossRef]
28. Shi, Y.-R.; Wang, K.-L.; Lou, Y.-H.; Zhang, D.-B.; Chen, C.-H.; Chen, J.; Ni, Y.-X.; Öz, S.; Wang, Z.-K.; Liao, L.-S. Unraveling the Role of Active Hydrogen Caused by Carbonyl Groups in Surface-Defect Passivation of Perovskite Photovoltaics. *Nano Energy* **2022**, *97*, 107200. [CrossRef]
29. Cai, Y.; Cui, J.; Chen, M.; Zhang, M.; Han, Y.; Qian, F.; Zhao, H.; Yang, S.; Yang, Z.; Bian, H.; et al. Multifunctional Enhancement for Highly Stable and Efficient Perovskite Solar Cells. *Adv. Funct. Mater.* **2021**, *31*, 2005776. [CrossRef]
30. Lin, Y.; Shen, L.; Dai, J.; Deng, Y.; Wu, Y.; Bai, Y.; Zheng, X.; Wang, J.; Fang, Y.; Wei, H. π-Conjugated Lewis Base: Efficient Trap-Passivation and Charge-Extraction for Hybrid Perovskite Solar Cells. *Adv. Mater.* **2017**, *29*, 1604545. [CrossRef]
31. Taguchi, M.; Suzuki, A.; Ueoka, N.; Oku, T. Effects of poly(Methyl Methacrylate) Addition to Perovskite Photovoltaic Devices. *AIP Conf. Proc.* **2019**, *2067*, 020018.
32. Jo, B.; Han, G.S.; Yu, H.M.; Choi, J.; Zhu, J.; Ahn, T.K.; Namkoong, G.; Jung, H.S. Composites of Cross-Linked Perovskite/Polymer with Sodium Borate for Efficient and Stable Perovskite Solar Cells. *J. Mater. Chem. A* **2022**, *10*, 14884–14893. [CrossRef]
33. Ochoa-Martinez, E.; Ochoa, M.; Ortuso, R.D.; Ferdowsi, P.; Carron, R.; Tiwari, A.N.; Steiner, U.; Saliba, M. Physical Passivation of Grain Boundaries and Defects in Perovskite Solar Cells by an Isolating Thin Polymer. *ACS Energy Lett.* **2021**, *6*, 2626–2634. [CrossRef]
34. Peng, J.; Khan, J.I.; Liu, W.; Ugur, E.; Duong, T.; Wu, Y.; Shen, H.; Wang, K.; Dang, H.; Aydin, E.; et al. A Universal Double-Side Passivation for High Open-Circuit Voltage in Perovskite Solar Cells: Role of Carbonyl Groups in Poly(methyl methacrylate). *Adv. Energy Mater.* **2018**, *8*, 1801208. [CrossRef]
35. Yang, F.; Lim, H.E.; Wang, F.; Ozaki, M.; Shimazaki, A.; Liu, J.; Mohamed, N.B.; Shinokita, K.; Miyauchi, Y.; Wakamiya, A.; et al. Roles of Polymer Layer in Enhanced Photovoltaic Performance of Perovskite Solar Cells via Interface Engineering. *Adv. Mater. Interfaces* **2018**, *5*, 1701256. [CrossRef]
36. Kim, H.; Lee, K.S.; Paik, M.J.; Lee, D.Y.; Lee, S.-U.; Choi, E.; Yun, J.S.; Seok, S.I. Polymethyl Methacrylate as an Interlayer Between the Halide Perovskite and Copper Phthalocyanine Layers for Stable and Efficient Perovskite Solar Cells. *Adv. Funct. Mater.* **2022**, *32*, 2110473. [CrossRef]
37. Choi, K.; Choi, H.; Min, J.; Kim, T.; Kim, D.; Son, S.Y.; Kim, G.-W.; Choi, J.; Park, T. A Short Review on Interface Engineering of Perovskite Solar Cells: A Self-Assembled Monolayer and Its Roles. *Sol. RRL* **2020**, *4*, 1900251. [CrossRef]
38. Bube, R.H. Trap Density Determination by Space-Charge-Limited Currents. *J. Appl. Phys.* **1962**, *33*, 1733–1737. [CrossRef]
39. Sworakowski, J.; Ferreira, G.F.L. Space-Charge-Limited Currents and Trap-Filled Limit in One-Dimensional Insulators. *J. Phys. D Appl. Phys.* **1984**, *17*, 135. [CrossRef]
40. Speirs, M.J.; Dirin, D.N.; Abdu-Aguye, M.; Balazs, D.M.; Kovalenko, M.V.; Loi, M.A. Temperature Dependent Behaviour of Lead Sulfide Quantum Dot Solar Cells and Films. *Energy Environ. Sci.* **2016**, *9*, 2916–2924. [CrossRef]
41. Ryu, S.; Nguyen, D.C.; Ha, N.Y.; Park, H.J.; Ahn, Y.H.; Park, J.-Y.; Lee, S. Light Intensity-dependent Variation in Defect Contributions to Charge Transport and Recombination in a Planar $MAPbI_3$ Perovskite Solar Cell. *Sci. Rep.* **2019**, *9*, 19846. [CrossRef] [PubMed]
42. Cao, Q.; Li, Y.; Zhang, H.; Yang, J.; Han, J.; Xu, T.; Wang, S.; Wang, Z.; Gao, B.; Zhao, J.; et al. Efficient and Stable Inverted Perovskite Solar Cells with Very High Fill Factors via Incorporation of Star-Shaped Polymer. *Sci. Adv.* **2021**, *7*, eabg0633. [CrossRef] [PubMed]

43. Lu, H.; Tian, W.; Cao, F.; Ma, Y.; Gu, B.; Li, L. A Self-Powered and Stable All-Perovskite Photodetector–Solar Cell Nanosystem. *Adv. Funct. Mater.* **2016**, *26*, 1296–1302. [CrossRef]
44. Xue, J.; Zhu, Z.; Xu, X.; Gu, Y.; Wang, S.; Xu, L.; Zou, Y.; Song, J.; Zeng, H.; Chen, Q. Narrowband Perovskite Photodetector-Based Image Array for Potential Application in Artificial Vision. *Nano Lett.* **2018**, *18*, 7628–7634. [CrossRef] [PubMed]
45. Li, C.; Wang, H.; Wang, F.; Li, T.; Xu, M.; Wang, H.; Wang, Z.; Zhan, X.; Hu, W.; Shen, L. Ultrafast and broadband photodetectors based on a perovskite/organic bulk heterojunction for large-dynamic-range imaging. *Light: Sci. Appl.* **2020**, *9*, 31. [CrossRef]
46. Wang, Y.; Liu, Y.; Cao, S.; Wang, J. A Review on Solution-Processed Perovskite/Organic Hybrid Photodetectors. *J. Mater. Chem. C* **2021**, *9*, 5302–5322. [CrossRef]
47. Guo, F.; Yang, B.; Yuan, Y.; Xiao, Z.; Dong, Q.; Bi, Y.; Huang, J. A Nanocomposite Ultraviolet Photodetector Based on Interfacial Trap-Controlled Charge Injection. *Nat. Nanotechnol.* **2012**, *7*, 798–802. [CrossRef]
48. Li, T.; Li, Q.; Tang, X.; Chen, Z.; Li, Y.; Zhao, H.; Wang, S.; Ding, X.; Zhang, Y.; Yao, J. Environment-Friendly Antisolvent Tert-Amyl Alcohol Modified Hybrid Perovskite Photodetector with High Responsivity. *Photonics Res.* **2021**, *9*, 781–791. [CrossRef]
49. Wang, S.; Li, T.; Li, Q.; Zhao, H.; Zheng, C.; Li, M.; Li, J.; Zhang, Y.; Yao, J. Inhibition of Buried Cavities and Defects in Metal Halide Perovskite Photodetectors via a Two-Step Spin-Coating Method. *J. Mater. Chem. C* **2022**, *10*, 7886–7895. [CrossRef]
50. Ma, N.; Jiang, J.; Zhao, Y.; He, L.; Ma, Y.; Wang, H.; Zhang, L.; Shan, C.; Shen, L.; Hu, W. Stable and Sensitive Tin-Lead Perovskite Photodetectors Enabled by Azobenzene Derivative for Near-Infrared Acousto-Optic Conversion Communications. *Nano Energy* **2021**, *86*, 106113. [CrossRef]